

The Different Dynamic Influences of Typhoon Kalmaegi on two Pre-existing Anticyclonic Ocean Eddies

Yihao He¹, Xiayan Lin^{1,2,*}, Guoqing Han¹, Yu Liu^{1,3} and Han Zhang^{2,3,*}

¹ Marine Science and Technology College, Zhejiang Ocean University, Zhoushan 316022, China;

² State Key Laboratory of Satellite Ocean Environment Dynamics, Second Institute of Oceanography, Ministry of Natural Resources, Hangzhou 310012, China;

³ Southern Marine Science and Engineering Guangdong Laboratory (Zhuhai), Zhuhai 519082, China

*Correspondence: Xiayan Lin (linxiayan@zjou.edu.cn) and Han Zhang (zhanghan@sio.org.cn)

Abstract: Using multi-source observational data and GLORYS12V1 reanalysis data, we conduct a comparative analysis of different responses of two warm eddies, AE1 and AE2 in the northern South China Sea to Typhoon Kalmaegi during September 2014. The findings of our research are as follows: (1) For horizontal distribution, the area and the sea surface temperature (SST) of AE1 and AE2 decrease by about 31% (36%) and 0.4 °C (0.6 °C). The amplitude, Rossby number (R_o =relative vorticity/Coriolis parameter) and eddy kinetic energy (EKE) of AE1 increases by 1.3 cm (5.7%), 1.4×10^{-2} (20.6%) and $107.2 \text{ cm}^2 \cdot \text{s}^{-2}$ (49.2%) after the typhoon, respectively, while AE2 weakens and the amplitude, Rossby number and EKE decreased by 3.1 cm (14.6%), 1.6×10^{-2} (26.2%) and $38.5 \text{ cm}^2 \cdot \text{s}^{-2}$ (20.2%), respectively. (2) In vertical direction, AE1 demonstrates enhanced convergence, leading to an increase in temperature and a decrease in salinity above 150 m. The response below the mixing layer depth (MLD) is particularly prominent (1.3 °C). In contrast, AE2 experiences cooling and a decrease in salinity above the MLD. Below the MLD, it exhibits a subsurface temperature drop and salinity increase due to the upwelling of cold water induced by the suction effect of the typhoon. (3) The disparity in the responses of the two warm eddies can be attributed to their different positions relative to Typhoon Kalmaegi. Warm eddy AE1, with its center located on the left side of the typhoon's path, experiences a positive work effect as the typhoon passes by. The negative wind stress curl in AE1 triggers a negative Ekman pumping velocity (EPV), further enhances by the converging sinking of the upper warm water, thereby strengthening AE1. On the other hand, warm eddy AE2, situates closer to the center of the typhoon, weakens due to the cold suction caused by the strong positive wind stress curl in the typhoon's center. Same polarity eddies may have different responses to typhoons, the distance between eddies and typhoons, eddies intensity and the background field need to be considered.

31 **1. Introduction**

32 Tropical cyclones (TCs), as they traverse the vast ocean, interact with oceanic mesoscale processes,
33 particularly with mesoscale eddies, representing a crucial aspect of air-sea interaction (Shay and Jaimes,
34 2010; Lu et al., 2016; Song et al., 2018; Ning et al., 2019; Sun et al., 2023). The South China Sea (SCS)
35 experiences an average of six TCs passing through each year (Wang et al., 2007), causing prominent
36 exchange of energy and mass between air and sea interface (Price, 1981). Meanwhile, due to the influence
37 of the Asian monsoon, intrusion of the Kuroshio Current, and complex topography, the Northern South
38 China Sea (NSCS) also encounters frequent eddy activities (Xiu et al., 2010; Chen et al., 2011). These
39 mesoscale oceanic eddies often play significant roles in mass and heat transportation and air-sea
40 interaction. This unique setting offers an exceptional opportunity to investigate the generation, evolution,
41 and termination of mesoscale eddies and their interaction with TCs.

42 On one hand, from a thermodynamic perspective, TCs derive their development and sustenance
43 energy from the ocean. Pre-existing mesoscale eddies play a crucial role in the feedback mechanism
44 between the ocean and TCs. Cyclonic eddies (cold eddies) enhance the sea surface cooling effect under
45 TCs conditions, resulting in TCs weakening, due to their thermodynamic structures and cold-water
46 entrainment processes that reduce the heat transfer from the sea surface to the TCs through air-sea
47 interaction (Ma et al., 2017; Yu et al., 2021). In contrast, anticyclonic eddies (warm eddies) suppress this
48 cooling effect, leading to TCs intensification (Shay et al., 2000; Walker et al., 2005; Lin et al., 2011;
49 Wang et al., 2018). Warm eddies have a thicker upper mixed layer, which stores more heat. When a TC
50 passes through a warm eddy, it increases sensible heat and water vapor in TC's center, which are closely
51 related to the TC's intensification (Wada and Usui, 2010; Huang et al., 2022). Furthermore, the
52 downwelling within warm eddies hinders the upwelling of cold water, reducing the apparent sea surface
53 cooling caused by the TCs. These processes weaken the oceanic negative feedback effect and help to
54 sustain or even strengthen TC's development. While from a dynamic perspective, TCs cause the
55 strengthening of cyclonic eddies, leading to positive potential vorticity anomalies, then accelerates the
56 currents and exacerbates global warming, ultimately further promotes TCs enhancement (Zhang et al,
57 2020).

58 On the other hand, TCs also have a notable impact on the intensity, size, and movement of mesoscale
59 eddies. In general, TCs strengthen cold eddies and can even lead to the formation of new cyclonic eddies

60 in certain situations (Sun et al., 2014), while TCs accelerate the dissipation of anticyclonic eddies (Zhang
61 et al., 2020). The strengthening effect of TCs on cold eddies is related to the positions between cold
62 eddies and TCs, the intensity of eddies, and TC-induced geostrophic response (Lu et al., 2016; Yu et al.,
63 2019; Lu et al., 2023). Cyclonic eddies on the left side of the TC track were more intensely affected by
64 the TC, and eddies with shorter lifespans or smaller radii are more susceptible to the influence of TCs.
65 The dynamic adjustment process of eddy and the upwelling induced by TC itself leads to changes in the
66 three-dimensional structure of the cyclonic eddies, including ellipse deformation and re-
67 axisymmetrization on the horizontal plane, resulting in eddy intensification. The presence of cold eddies
68 not only exacerbates the sea surface cooling in cold eddy region but also accompanies a decrease in sea
69 level anomaly (SLA), deepening of the mixed layer, a strong cooling in the subsurface, increased
70 chlorophyll-a concentration within the eddy, and substantial increases in EKE and available potential
71 energy (Shang et al., 2015; Liu and Tang, 2018; Li et al., 2021; Ma et al., 2021).

72 Generally, typhoons lead to a reduction of warm eddies, while the sea surface cooling is not
73 significant, typically within 1°C. However, there is a noticeable cooling and increased salinity in the
74 subsurface layer, accompanied by an upward shift of the 20°C isotherm, a decrease in heat and kinetic
75 energy (Lin et al., 2005; Liu et al., 2017; Huang and Wang, 2022). Lu et al. (2020) propose that typhoons
76 primarily generate potential vorticity input through the geostrophic response. When a TC passes over an
77 eddy, there is a significant positive wind stress curl within the TC's maximum wind radius, which induces
78 upwelling in the mixed layer due to the divergence of the wind-driven flow field. This upward flow
79 compresses the thickness of the isopycnal layers below the mixed layer, resulting in a positive potential
80 vorticity anomaly. By analyzing the time series of ocean kinetic energy, available potential energy (APE),
81 vorticity budget, and potential vorticity (PV) budget, Rudzin and Chen (2022) find that the positive
82 vertical vorticity advection caused the TC to eliminate the warm eddy from bottom to top after passing
83 through. Under the interaction of the strong TC wind stress in the eye area of the TC and the subsurface
84 ocean current field, the early-onset of a near-inertial wake caused the disappearance of the warm eddy.
85 However, the projection of TC wind stress onto the eddy and the relative position of the warm eddy to
86 the TC can lead to different responses. According to the classical description of TC-induced upwelling,
87 strong upwelling occurs within twice the maximum wind radius of the TC center, while weak subsidence
88 exists in the vast area outside the upwelling region (Price, 1981; Jullien et al., 2012). The warm eddy
89 locates directly beneath the TC's path weakens due to the cold suction caused by the TC's center.

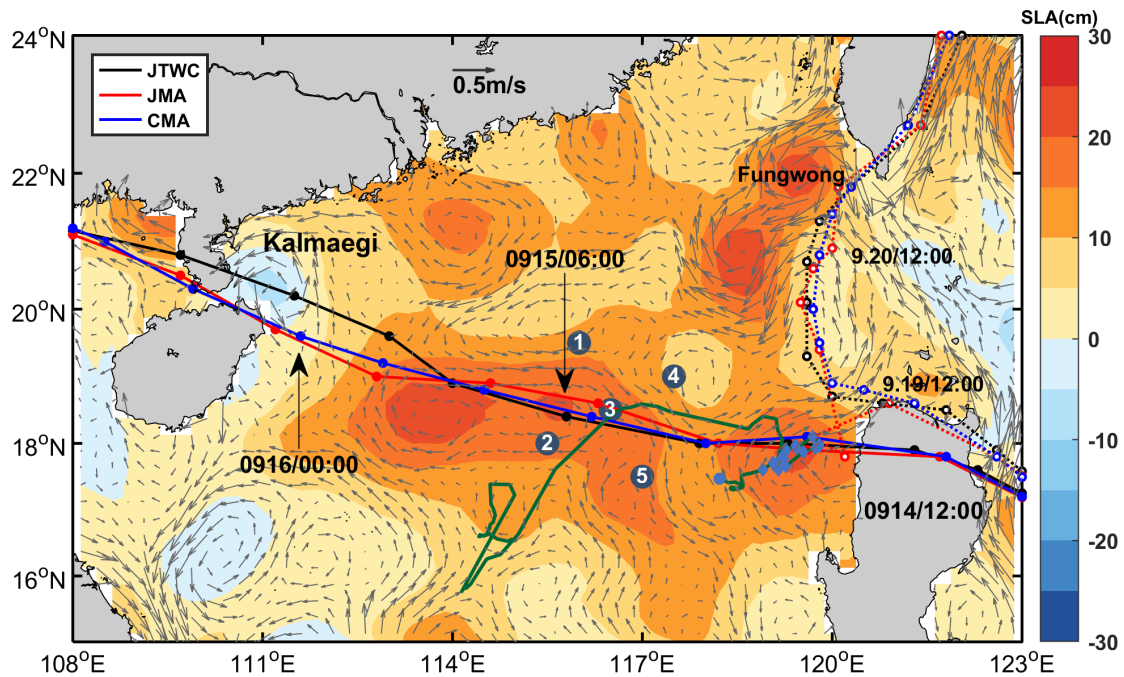
90 However, for warm eddies locate beyond twice the maximum wind radius, they are influenced by the
91 TC's wind stress curl and the downwelling within the eddy itself, resulting in the convergence of warm
92 water in the upper layers of the eddy, an increase in mixed layer thickness, and an increase in heat content,
93 leading to a warming response to the TC (Jaimes and Shay, 2015).

94 The NSCS frequently experiences intense TCs, coinciding with notable mesoscale eddies activity in
95 the region. Based on in-situ datasets, multi-platform satellite measurements, and GLORYS12V1
96 reanalysis data, we investigate the influence of two anticyclonic eddies on upper ocean responses to
97 Typhoon Kalmaegi. This marks our initial endeavor to characterize the distinct physical variations
98 induced by TCs within two eddies of the same polarity. This effort contributes to a deeper understanding
99 of the role played by mesoscale eddies in modulating interactions between TCs and the ocean. Section 2
100 provides an overview of the data and methods utilized in this research. Section 3 analyzes the physical
101 parameters of warm eddies, vertical temperature and salinity variations, and explores the different
102 responses of warm eddies both inside and outside the typhoon affected region. Section 4 offers a
103 comprehensive discussion and Section 5 gives a summary.

104 **2. Data and Methods**

105 **2.1. Data**

106 The six-hourly best-track typhoon datasets are obtained from the Joint Typhoon Warning Center
107 (JTWC, <http://www.usno.navy.mil/JTWC>, last access: 3 February, 2021), the Japan Meteorological
108 Agency (JMA, <https://www.jma.go.jp/jma/jma-eng/jma-center/rsmc-hp-pub-eg/besttrack.html>, last
109 access: 3 February, 2021), and the China Meteorological Administration (CMA,
110 <http://tcdata.typhoon.gov.cn>, last access: 3 February, 2022). The data contain the TCs' center locations,
111 the minimum central pressure, maximum sustained wind speed, and intensity category. The translation
112 speed of typhoons is calculated by dividing the distance travelled by each typhoon within a 6-hour
113 interval by the corresponding time. In this paper, Typhoon Kalmaegi and tropical storm Fung-wong are
114 studied (Fig. 1).



116 **Figure 1.** The tracks of Typhoon Kalmaegi (solid lines with dots) and tropical storm Fung-wong (dashed lines with
 117 hollow dots) as provide by the Joint Typhoon Warning Center (JTWC, black), Japan Meteorological Agency (JMA,
 118 red), and China Meteorological Administration (CMA, blue). The colour shading represents the sea surface level
 119 anomaly on 13 September, 2014, while the gray arrows illustrate the geostrophic flow field. The numbered blue dots
 120 represent the positions of the five buoy/mooring stations, the green line illustrates the trajectory of Argo 2901469,
 121 and the blue diamond's mark the positions of Argo 2901469 inside the eddy AE2 from 26 August 2014 to 25 October
 122 25, 2014.

123 The daily Sea Level Anomaly (SLA) and geostrophic current data provide by Archiving, Validation,
 124 and Interpretation of Satellite Data in Oceanography (AVISO) product (CMEMS,
 125 <https://marine.copernicus.eu/>, last access: 14 February, 2022). This dataset combines satellite data from
 126 Jason-3, Sentinel-3A, HY-2A, Saral/AltiKa, Cryosat-2, Jason-2, Jason-1, T/P, ENVISAT, GFO, and
 127 ERS1/2. The spatial resolution of the product is $1/4^\circ \times 1/4^\circ$, the period from 1 September to 30 September
 128 2014 was used.

129 The daily Sea Surface Temperature (SST) data used in this study is derived from the Advanced Very
 130 High-Resolution Radiometer (AVHRR) product data provided by the National Oceanic and Atmospheric
 131 Administration (NOAA). The data is obtained from the Physical Oceanography Distributed Active
 132 Archive Center (PODAAC) at the NASA Jet Propulsion Laboratory (JPL)
 133 (ftp://podaac.jpl.nasa.gov/documents/dataset_docs/avhrr_pathfinder_sst.html, last access: 16 March,
 134 2022). The spatial resolution of the data is $1/4^\circ \times 1/4^\circ$.

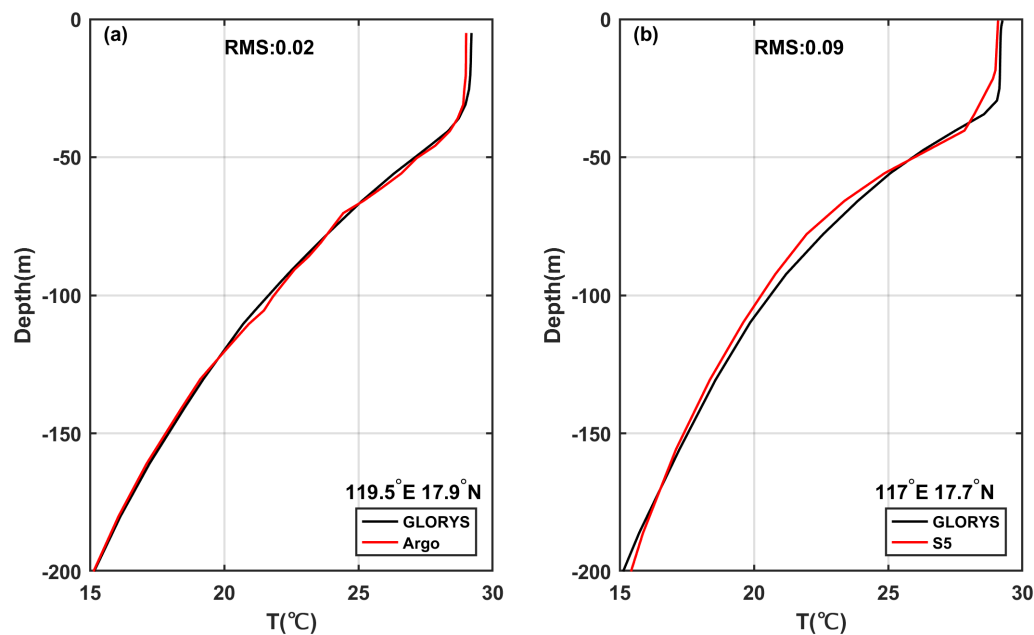
135 Argo data, including profiles of temperature and salinity from surface to 2000 m depth are obtained
 136 from the real-time quality-controlled Argo data base (Euro-Argo, <https://dataselection.euro-argo.eu/>, last
 137 access: 4 April, 2022). We select Argo float number 2901469, situated in an ocean anticyclonic eddy and
 138 in close proximity to typhoon Kalmaegi, both before and after the typhoon's passage in 2014. Profiles of
 139 this Argo are also used to validate the vertical distribution of temperature and salinity from
 140 GLORYS12V1.

141 For this study, we also utilize in-situ data from a cross-shaped array consisting of five stations,
142 comprising five moored buoys and four subsurface moorings (refer to Fig. 1). More specific information
143 can be found in Zhang et al. (2016). To investigate the impact of the typhoon on a warm eddy, we select
144 the temperature and salinity data from Station 5, situated along the left track of Kalmaegi.

145 The wind speed data is sourced from the European Centre for Medium-Range Weather Forecasts
146 (ECMWF) ERA-Interim reanalysis assimilation dataset ([https://apps.ecmwf.int/datasets/data/interim-
147 full-daily/levtype=sfc/](https://apps.ecmwf.int/datasets/data/interim-full-daily/levtype=sfc/), last access: 5 January, 2023). This dataset is widely used for weather analysis
148 and numerical forecasting. The wind field data used in this study primarily focuses on the reanalysis data
149 of surface winds at a height of 10 meters above sea level for TCs. The selected data has a spatial
150 resolution of $1/4^\circ \times 1/4^\circ$ and a temporal resolution of 6 hours, with four updates per day (00:00, 06:00,
151 12:00, and 18:00 UTC). The data utilized corresponds to September 2014.

152 The Global Ocean Reanalysis Product GLOBAL_REANALYSIS_PHY_001_030 (GLORYS12),
153 provided by the Copernicus Marine Environment Monitoring Service (CMEMS,
154 <https://marine.copernicus.eu/>, last access: 23 March, 2022) is used in this study too. This reanalysis
155 product utilized the NEMO 3.1 numerical model coupled with the LIM2 sea ice model, and forced with
156 ERA-Interim atmospheric data. The model assimilated along-track altimeter data from satellite
157 observations (Pujol et al., 2016), satellite sea surface temperature data from AVHRR, sea ice
158 concentration from CERSAT (Ezraty et al., 2007), and vertical profiles of temperature and salinity from
159 the CORAv4.1 database (Cabanes et al., 2012). The temperature and salinity biases were corrected using
160 a 3D-VAR scheme. The horizontal resolution is $1/12^\circ \times 1/12^\circ$, and it has 50 vertical levels. The
161 temperature and salinity **from** 1 September to 30 September 2014 **were** chosen to study.

162 GLORYS12V1 is a widely used and applicable dataset, to evaluate its temperature profiles, the Argo
163 profiles and in-situ data of Station 5 were compared (Fig. 2). The GLORYS12V1 data exhibit good
164 agreement with Argo profiling floats, the maximum difference between them is less than 0.2°C , the Root
165 Mean Square (RMS) is 0.02. However, there are some discrepancies between the GLORYS12V1 and
166 the Station 5 data, with the largest difference occurring at the depths of 30 m (mixed layer) and 78 m
167 (thermocline), both differing by 0.6°C , while below 150 m, the difference is quite small. The RMS is
168 0.09. The RMS between GLORYS12V1 and Station 2 (Station 4) is 0.14 (0.10) (Figures not shown).
169 Because the GLORYS12V1 assimilates with Argo data and the vertical resolution of upper 100 m in
170 Argo profile is 5 m, but the vertical interval of buoy array is 20 m. Therefore, the large deviations exist
171 at mixed layer and thermocline during the typhoon in in-situ data of Station 5. Overall, GLORYS12V1
172 reproduces the observed ocean temperature accurately, it is reasonable to use it to investigate the vertical
173 response of anticyclonic eddies by typhoon Kalmaegi.



175 **Figure 2.** Evaluation of GLORYS12V1 data performance during September 2014. **(a)** Vertical monthly mean
 176 temperature within the anticyclonic eddy AE2 (119.5°E 17.9°N) as measured by Argo float 2901469. **(b)**
 177 Comparison of vertical monthly mean temperature recorded at Station 5 (117°E 17.7°N).

178 2.2. Methods

179 Vorticity is a vector that characterizes the local rotation within a fluid flow. Mathematically, it is
 180 defined as the curl of the velocity vector. In most cases, when referring to vorticity, it specifically pertains
 181 to the vertical component of the vorticity. It is calculated from:

$$182 \quad \zeta = \frac{\partial v}{\partial x} - \frac{\partial u}{\partial y} . \quad (1)$$

183 u and v are the zonal (eastward) and meridional (northward) geostrophic velocities, respectively. They
 184 are derived from altimeter sea level anomaly data (η):

$$185 \quad u = -\frac{g}{f} \frac{\partial \eta}{\partial y} , v = \frac{g}{f} \frac{\partial \eta}{\partial x} . \quad (2)$$

186 Here, g is the acceleration of gravity, f is the Coriolis frequency. Vorticity is considered a
 187 fundamental characteristic of mesoscale eddies, positive vorticity signifies cyclonic eddies, while
 188 negative vorticity indicates anticyclonic eddies.

189 The Rossby number (R_o) is a dimensionless number describing fluid motion, and it is the ratio of
 190 relative vorticity to planetary vorticity, reflecting the relative importance of local non-geostrophic motion
 191 to large-scale geostrophic motion. The larger the Rossby number, the stronger the local non-geostrophic
 192 effect, and the definition of this parameter is:

$$193 \quad R_o = \frac{\zeta}{f} . \quad (3)$$

194 Eddy Kinetic Energy (EKE) is a measure of the energy associated with mesoscale eddies, which
 195 indicates the intensity of eddies. It is typically calculated using the anomalies of the geostrophic velocity:

$$196 \quad EKE = \frac{1}{2}(u'^2 + v'^2) , \quad (4)$$

197 where u' represents the anomaly of the geostrophic zonal (eastward) velocity, v' represents the anomaly
 198 of the meridional (northward) velocity.

199 To evaluate the impact of a typhoon on an anticyclonic eddy, the calculation begins with determining
 200 the wind stress:

$$201 \quad \vec{\tau} = \rho_a C_d U_{10} \overrightarrow{U}_{10} , \quad (5)$$

202 where ρ_a is the air density, assumed to be a constant value of 1.293 kg m^{-3} , U_{10} represents the 10-
 203 meter wind speed. And C_d is the drag coefficient at the sea surface (Oey et al., 2006):

$$204 \quad C_d \times 1000 = \begin{cases} 1.2 & U_{10} \leq 10m \text{ s}^{-1} \\ 0.49 + 0.65U_{10} & 11 \leq U_{10} < 19m \text{ s}^{-1} \\ 1.364 + 0.234U_{10} - 0.00023158U_{10}^2 & 19 \leq U_{10} \leq 100m \text{ s}^{-1} \end{cases} . \quad (6)$$

205 The wind stress curl is calculated by (Kessler, 2006):

$$206 \quad curl(\vec{\tau}) = \frac{\partial \tau_y}{\partial x} - \frac{\partial \tau_x}{\partial y} , \quad (7)$$

207 where τ_x and τ_y are the eastward and northward wind stress vector components, respectively. The curl
 208 represents the rotation experienced by a vertical air column in response to spatial variations in the wind
 209 field.

210 The Ekman pumping velocity (EPV) represents the ocean upwelling rate, which can be used to study
 211 the contribution of typhoons to regional ocean upwelling. Positive means upwelling, negative represents
 212 downwelling:

$$213 \quad EPV = curl\left(\frac{\vec{\tau}}{\rho f}\right) , \quad (8)$$

214 where the wind stress is obtained from Eq. (7), ρ is seawater density, the value is 1025 kg m^{-3} , and f
 215 is the Coriolis frequency.

216 The buoyancy frequency is a measure of the degree to which water is mixed and stratified. In a stable
 217 temperature stratification, the fluid particles move in the vertical direction after being disturbed, and the
 218 combined action of gravity and buoyancy always makes them return to the equilibrium position and
 219 oscillate due to inertia. When $N^2 < 0$, the water is in an unstable state:

$$220 \quad N^2 = -\frac{g}{\rho} \frac{\partial \rho}{\partial z} \quad (9)$$

221 where ρ is seawater density, g is the acceleration of gravity, and z is the depth.

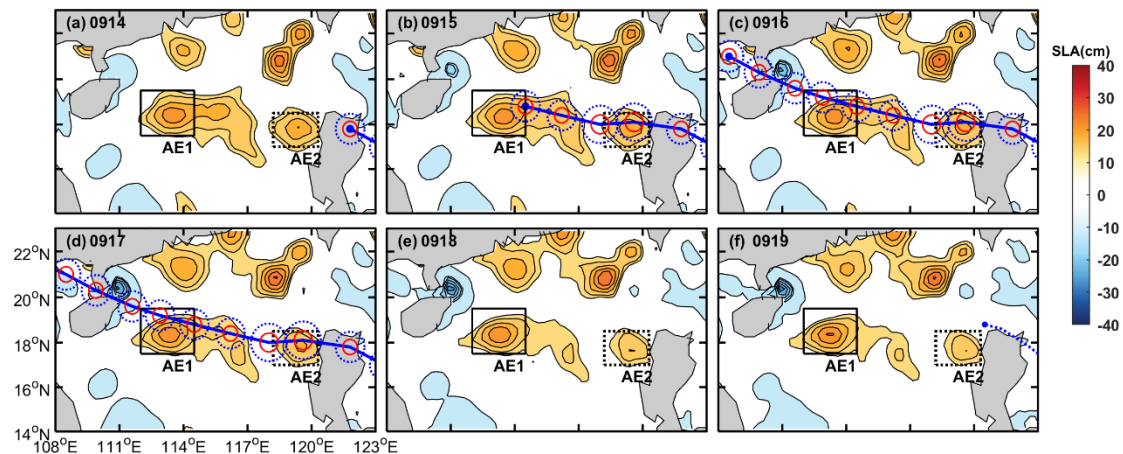
222 **3. Results**

223 **3.1. Typhoon and pre-existing eddies in the NSCS**

224 **3.1.1. Track of Typhoon Kalmaegi and tropical storm Fung-wong**

225 Typhoon Kalmaegi strengthens into a typhoon by 1200 UTC on 13 September and emerged over the
226 warm waters of the Northern South China Sea (NSCS) by 1500 UTC on 14 September, with maximum
227 sustained winds of $33 \text{ m}\cdot\text{s}^{-1}$ (Fig. 3-4). During this period, the NSCS experiences predominantly weak
228 vertical wind shear and is characterized by multiple anticyclonic warm eddies (Fig. 3). Subsequently,
229 Typhoon Kalmaegi undergoes two rapid intensification phases between 15 and 16 September. The first
230 intensification occurs at 0000 UTC on 15 September, propelling Kalmaegi to category 1 status with
231 surface winds surpassing $35 \text{ m}\cdot\text{s}^{-1}$. By 1200 UTC on 15 September, Kalmaegi experiences a second, even
232 more rapid intensification, with winds reaching $40 \text{ m}\cdot\text{s}^{-1}$ in less than 12 hours. Throughout this
233 intensification stage, Kalmaegi encounters two warm eddies: anticyclonic eddy AE1, is positioned to the
234 left of the typhoon's path, with its core situates on the periphery of the typhoon's two-times maximum
235 wind radius (Fig.3c-d). AE1 has a lifespan of 105 days from 26 June to 8 October and is positioned at
236 17°N - 20°N , 113°E - 116°E . AE2 precisely intersecting with the typhoon's trajectory, and its core nearly
237 coincides with the maximum wind radius of the typhoon (Fig.3b-d). It has a lifespan of 89 days from 24
238 August to 20 November and is located at 17°N - 19°N , 118°E - 120°E . Kalmaegi makes landfall on Hainan
239 Island at 0300 UTC on 16 September, with a minimum central pressure of 960 hPa and a maximum wind
240 speed of $40 \text{ m}\cdot\text{s}^{-1}$. After landfall, Typhoon Kalmaegi gradually weakens and dissipates. During its
241 crossing of the NSCS, the five mooring stations are affected. Stations 1 and 4 are on the right side of
242 Typhoon Kalmaegi's track, while Stations 2 and 5 are on the left side. Unfortunately, the wire rope of the
243 buoy at Station 3 is destroyed by Kalmaegi, resulting in missing data from 15 September. Among the
244 stations, Station 5 is on the left of typhoon track and outside AE2, so its data is used in our study.

245 Tropical storm Fung-wong initially moves quickly in a northwest direction after formation. On 19
246 September, it enters the Luzon Strait and decelerates. It makes landfall in Taiwan on the 21 September
247 and subsequently lands in Zhejiang on the 22 September before gradually dissipating. When crossing the
248 Luzon Strait at 1200 UTC on 19 September, anticyclonic eddy AE2 is on the left side of Fung-wong,
249 with a distance of just over 100 km from its center.



251 **Figure 3.** The variations in sea level anomaly before and after Typhoon Kalmaegi moved over the anticyclonic eddies
 252 AE1 and AE2 between 14 September and 19 September (a-f). The black solid rectangle represents the area of AE1,
 253 while the black dashed rectangle represents the area of AE2. The blue solid line depicts the path of Typhoon
 254 Kalmaegi, the solid red and dashed blue circles are the one- and two-times maximum wind radius of the typhoon,
 255 while the blue dotted line in (f) is the path of tropical storm Fung-wong (best-track data sourced from CMA).

256 3.1.2. Eddy characteristics distribution

257 Satellite SLA measurements have proven to be highly effective and widely used for identifying and
 258 quantifying the intensity of ocean eddies (Li et al., 2014). In Fig. 3, two warm eddies with clear positive
 259 (>13 cm) SLA are observed along the Typhoon Kalmaegi's track. During the period of 15 to 16
 260 September, the typhoon passes over two warm anticyclonic eddies, AE1 and AE2. Before the typhoon,
 261 AE1 is the most prominent eddy in the SCS, with an amplitude of 23.0 cm, and a radius of 115.5 km.
 262 AE2, locates west of Luzon Island, exhibits an amplitude of 21.2 cm, with a radius of approximately
 263 65.5 km. Tracing back to 2 months (figure is not shown), AE1 propagates slowly westward with about
 264 $0.1 \text{ m}\cdot\text{s}^{-1}$, while AE2 is generated on 24 August. During 14 to 19 September, the amplitude of AE1
 265 increases 1.3 cm. The area of the AE1 decreases by approximately 31% from $1.3 \times 10^5 \text{ km}^2$ to 9.1×10^4
 266 km^2 and splits into two eddies. When Typhoon Kalmaegi crosses the core of AE2 at 1500 UTC on 14
 267 September, and tropical storm Fung-wong moves over the northeast of AE2 at 1200 UTC on 19
 268 September, the amplitude decreases by 3.1 cm. The area of the AE2 decreases by approximately 36%
 269 from $4.2 \times 10^4 \text{ km}^2$ to $2.7 \times 10^4 \text{ km}^2$.

270 Because of intense solar radiation in September, the SST in the SCS is generally above 28.5°C prior
 271 to the arrival of Typhoon Kalmaegi (Fig. 4a). As a fast-moving typhoon with a mean moving speed of
 272 over $8 \text{ m}\cdot\text{s}^{-1}$, Kalmaegi induces a larger cooling area and intensity on the right side of its path compared
 273 to the left side (Price, 1981). During the passage of Kalmaegi, the lowest SST on the right side of typhoon
 274 decreases to 27.2°C . Even after the typhoon has passes, a cold wake can still be observed on the right
 275 side of its path, persisting for over a week (Fig. 4c).

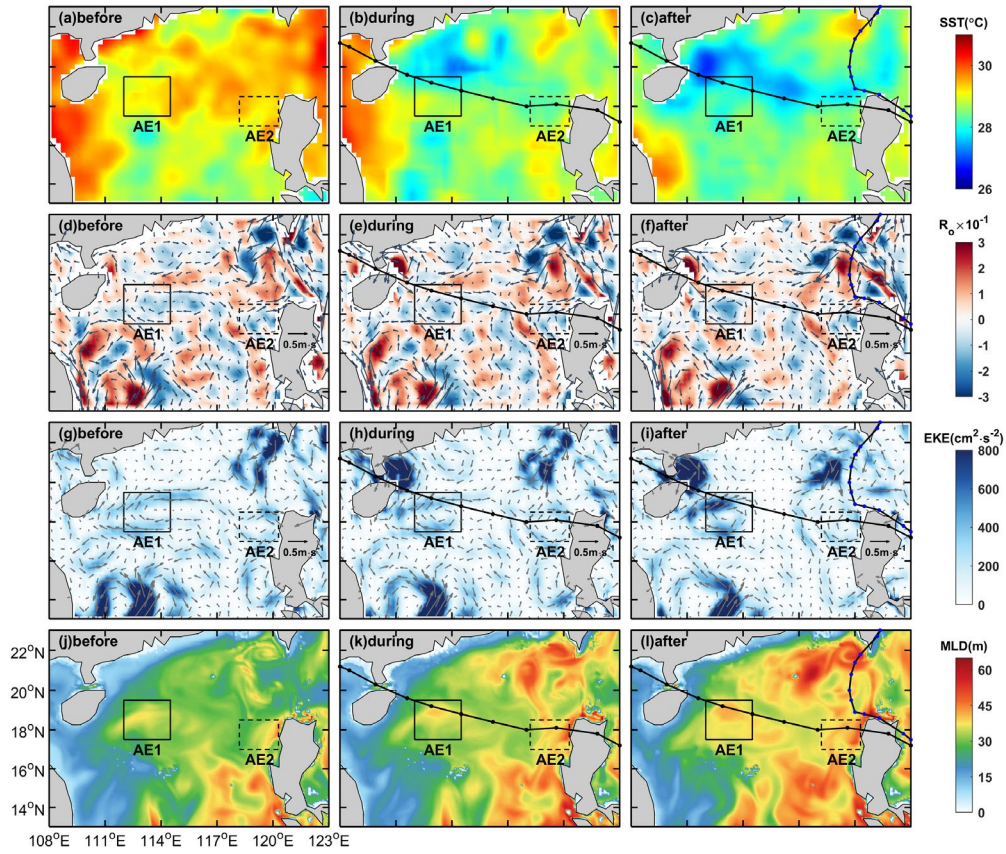
276 Mesoscale eddies, due to their special thermodynamic structure and varying positions in relation to
 277 the TC, can modulate distinct sea surface temperature changes and exhibit different characteristics. The
 278 pre-existing warm eddy AE1 begins to cool down before Kalmaegi reached the NSCS, dropping to

279 28.4°C on 14 September. During this period, the mean SST within AE1 increases slightly to 28.6 °C (Fig.
280 5a). However, as cooler water from the right side of the typhoon track is subsequently advected into the
281 AE1 region (Fig. 4c), the SST decreases and reaches 28.0 °C on September 19, which is 0.4°C lower
282 than that before the typhoon. The average SST drop in AE2 is relatively evident, with SST starting to
283 decline before 14 September and reaching its lowest temperature (28.1°C) on 15 September, 0.6 °C lower
284 than that before the typhoon (Fig. 5e). On 16 September, the SST within AE2 begins to recover, but it
285 starts to cool again on 18 September due to the influence of Fung-wong.

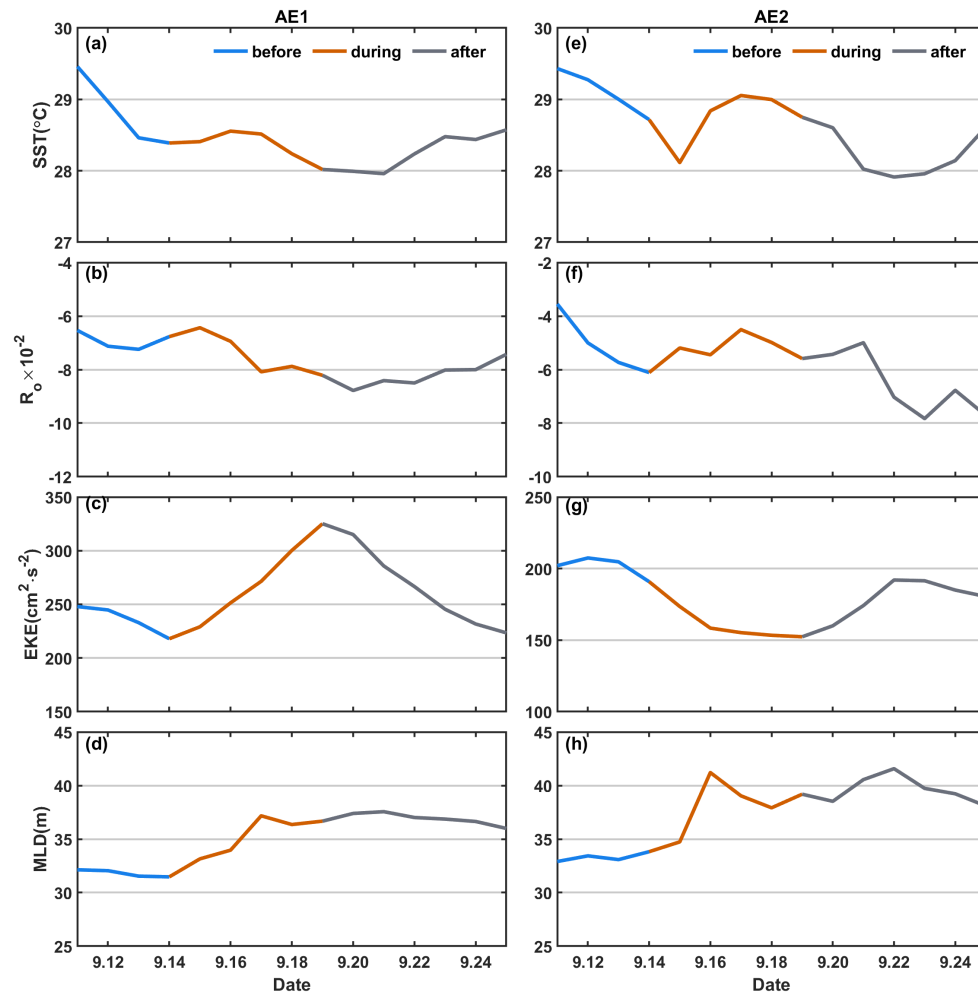
286 Then we compare the Ro and EKE of AE1 and AE2 before, during and after typhoon. Before being
287 influenced by the typhoon, the warm eddy AE1 exhibits a more scattered distribution of negative Ro due
288 to its edge structure, and the EKE values at the eddy boundary are relatively high (Fig. 4d, g). As the
289 typhoon passes through the eddy, the Ro and EKE of AE1 starts to increase. On 19 September, the
290 average Ro within AE1 reaches a value of -8.2×10^{-2} , at the same time, the average EKE increases to its
291 maximum value of $325.0 \text{ cm}^2 \cdot \text{s}^{-2}$. The variation trend of R_o and EKE within the eddy is consistent,
292 increasing from the passage of the typhoon and starting to recover on 20 September (Fig. 5b-c). This
293 indicates that although the area of the warm eddy AE1 decreased under the influence of the typhoon, its
294 intensity increases. On the other hand, for warm eddy AE2, both R_o and EKE decreases after the typhoon
295 passage, with the Ro decreasing to -4.5×10^{-2} on 17 September and the EKE decreasing to $152.0 \text{ cm}^2 \cdot \text{s}^{-2}$
296 on the 19 September, followed by a recovery (Fig. 5f-g). Unlike AE1, AE2 weakens in intensity under
297 the influence of the typhoon.

298 During the passage of the typhoon, enhances mixing driven by wind stress and increases vertical
299 shear result in a deepening of the MLD, which further strengthens the mixing between the deep cold
300 water and the upper warm water (Shay and Jaimes, 2009). To avoid a large part of the strong diurnal
301 cycle in the top few meters of the ocean, 10 m is set as the reference depth (De Boyer Montégut, 2004).
302 A 0.5 °C threshold difference from 10 m depth is calculated and defines as the MLD (Thompson and
303 Tkalic, 2014). Prior to the influence of Typhoon Kalmaegi, the MLD in the AE1 and AE2 regions is
304 deeper (Fig. 4j), with the average MLDs of 32 m and 33 m, respectively. Starting from 14 September,
305 the MLDs are influenced by Typhoon Kalmaegi, with the MLD of AE1 deepening to 37 m and that of
306 AE2 increasing to 41 m, representing a deepening of 5 m and 8 m, respectively (Fig. 5d, h).

307 Overall, Typhoon Kalmaegi likely exerts distinct impacts on the two warm eddies. Despite both AE1
308 and AE2 experiencing a decrease in their respective areas by approximately one-third, accompanied by
309 deepening of the MLD, the amplitude of SLA within AE1 increases by 1.3 cm, whereas AE2 witnesses
310 a decrease of about 3.1 cm in its amplitude. Furthermore, the SST, Rossby number and EKE within AE1
311 and AE2 exhibits contrasting patterns.



313 **Figure 4.** The spatial distribution of SST, R_o , EKE, and MLD before, during and after the passage of TCs. The
 314 time periods of 10-13, 15-16 and 19-22 September are designated as stages before, during and after Kalmaegi,
 315 respectively. The path of Typhoon Kalmaegi is depicted by a black solid line with black dots, while the path of
 316 tropical storm Fung-wong is represented by a black solid line with blue dots in the third column. The solid and
 317 dashed boxes correspond to AE1 and AE2, respectively.



319 **Figure 5.** The time series of sea surface temperature (SST), R_0 , eddy kinetic energy, and mixed layer depth (MLD)
 320 within the warm eddies' regions (black solid and dashed boxes in Fig. 4). The first column is variables of AE1, the
 321 second column is for AE2.

322 3.2 Upper-ocean vertical thermal and salinity structure of eddies

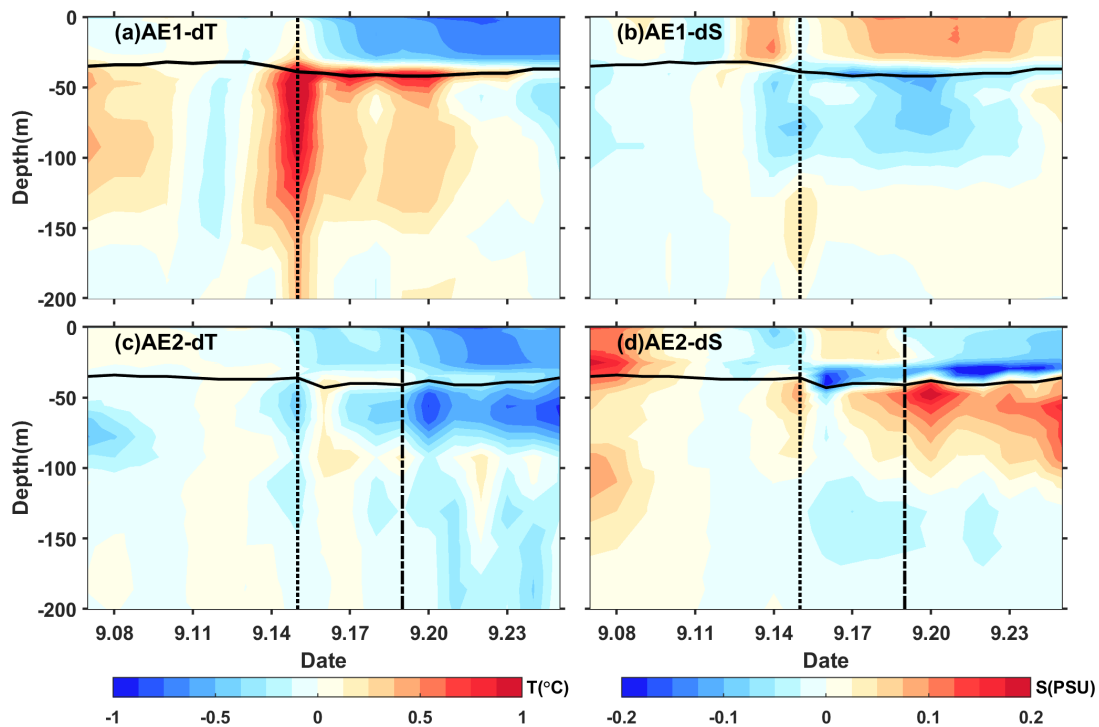
323 We conduct further analysis on the vertical temperature and salinity structure of the warm eddies
 324 AE1 and AE2 before and after the Typhoon Kalmaegi using GLORYS12V1 data. **During the typhoon's**
 325 **passage on 15 September**, the temperature above the MLD within AE1 increases by approximately 0.1 °C,
 326 while the salinity decreases by 0.02 psu (Fig. 6). Below the MLD, the temperature shows a significant
 327 increase, reaching a maximum temperature rise of 1.3 °C. Correspondingly, the salinity below the MLD
 328 exhibits a decrease of 0.05 psu. Vertical temperature on Kalmaegi's arrival day **shows** warm pattern from
 329 surface to 200 m, the salinity **shows** "fresher-saltier" pattern. These changes lead to a deepening of the
 330 isodensity by 15 m and a decrease in buoyancy frequency N^2 (Fig. 7a-b), indicating convergence and
 331 downwelling within the centre of the warm eddy AE1. **The near-inertial waves propagate downward**
 332 **from surface to 200m from this period (Zhang et al, 2017). The transfer of energy from anticyclonic eddy**
 333 **to near-inertial waves is the main reason for the downward propagation and longtime persistence of near-**
 334 **inertial energy (Chen et al, 2023).**

335 After 15 September, the temperature above the MLD decreases, and the salinity shows an increase
 336 (Fig. 6a-b), resulting in the uplift of the 1021 kg.m⁻³ isodensity to the sea surface (Fig. 7a-b). The
 337 subsurface warming and salinity reduction gradually weakens after the Typhoon Kalmaegi but persists
 338 for about a week after the typhoon's passage until 22 September. During this period, vertical temperature
 339 pattern becomes "cool-warm" at the center of AE1, and the salinity distribution pattern becomes "saltier-
 340 fresher-saltier". This persistence can be attributed to the intensified stratification around the MLD, with
 341 N² around 9.0×10⁻⁴s⁻² (Fig. 7b). The increased stability inhibits vertical mixing, restrains the exchange
 342 of heat and salinity, and leads to smoother density gradients above the MLD (Fig. 7a).

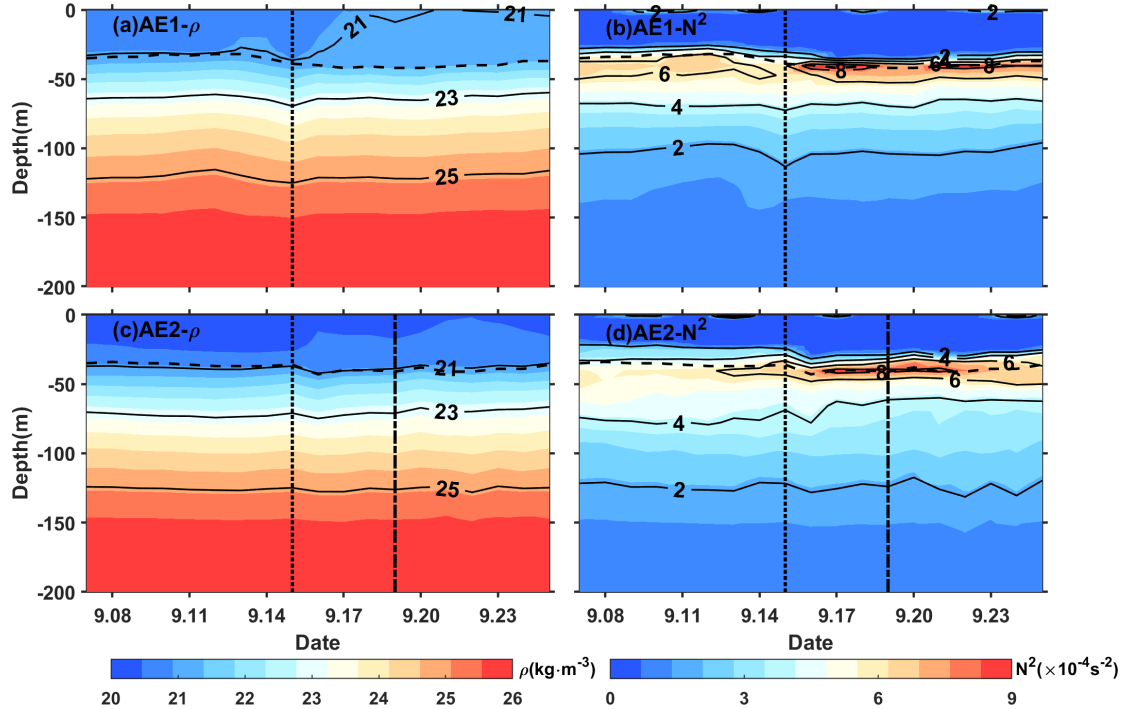
343 The vertical temperature and salinity structure of AE2 exhibits an opposite trend. During the typhoon
 344 passage on 15 September, AE2 also experiences a cooling trend of 0.2 °C, with a decrease in salinity of
 345 0.04 psu above the MLD. Below the MLD, the temperature shows a consistent decrease, with a change
 346 of less than 0.5 °C within the subsurface. Correspondingly, the salinity exhibits an increase of
 347 approximately 0.08 psu (Fig. 6c-d). The slightly upward shift of the isodensity (Fig. 7c) suggests the
 348 possibility of cold-water upwelling induced by the suction effect of the typhoon. The temperature
 349 decreases and salinity increases below the MLD are primarily driven by upwelling processes.

350 Furthermore, when the tropical storm Fung-wong passes through AE2 on 19 September (dashed line
 351 in Fig. 6c-d), the decreasing trend of subsurface temperature becomes more pronounced, and the
 352 subsurface salinity exhibits a significant increase. AE2 is more significantly influenced by tropical storm
 353 Fung-wong. It presents stable stratification with N² around 8.4×10⁻⁴s⁻² at a depth of 42 m, creating a
 354 barrier layer that prevents the intrusion of high-salinity cold water from the lower layers into the mixed
 355 layer (Yan et al., 2017).

356



358 **Figure 6.** The timeseries of vertical temperature and salinity anomalies in the center of AE1(a,b) and AE2 (c,d).
 359 The anomalies were calculated relative to the average value of 10-13 September. The vertical black dotted line
 360 indicates the Typhoon Kalmaegi's passage, while the vertical black dashed line represents the passage of tropical
 361 storm Fung-wong. The black solid line is the MLD.



363 **Figure 7.** Same as Fig. 7, but for density and buoyancy frequency (N^2).

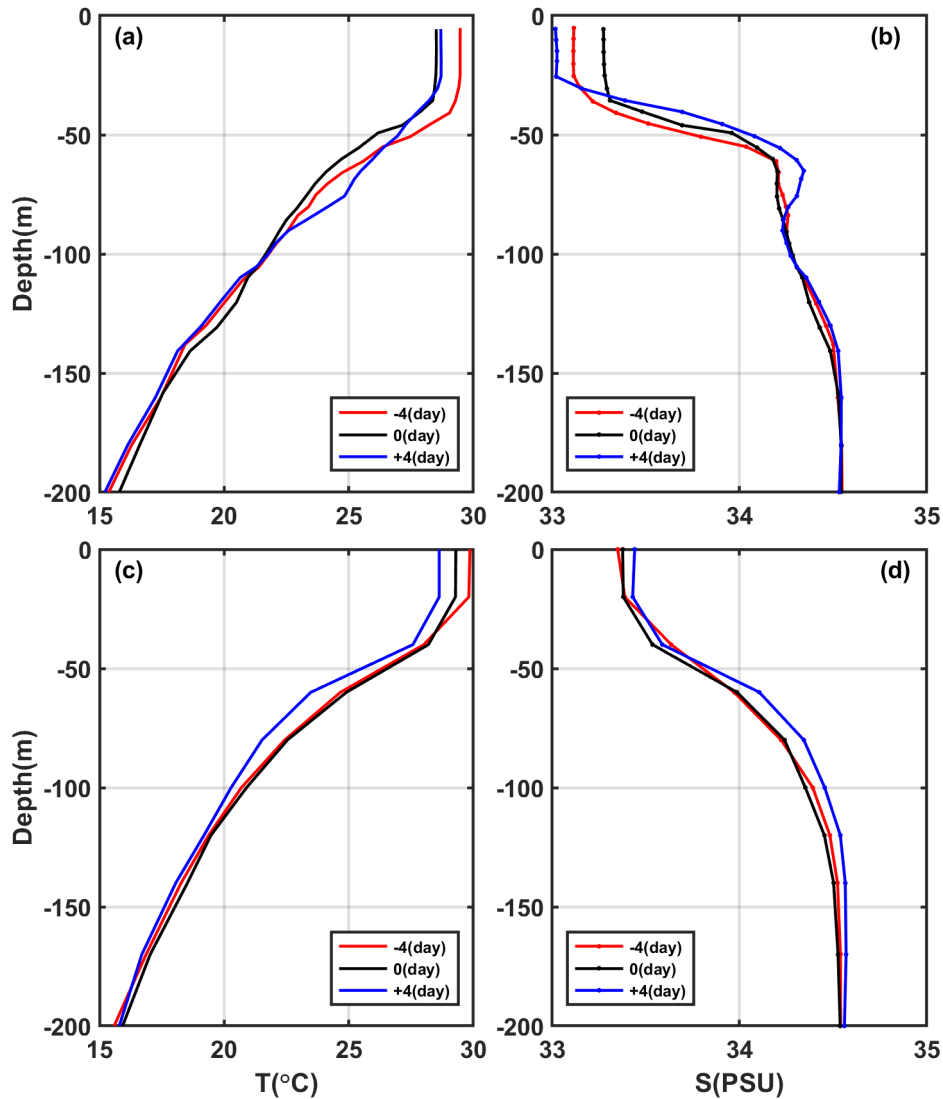
364 3.3 Comparison of the response between eddies and non-eddies areas

365 To investigate the contrasting response of warm eddies and the non-eddies background to Typhoon
 366 Kalmaegi, we conduct a comparative analysis of vertical temperature and salinity profiles in these two
 367 areas. Unfortunately, there is no Argo data around AE1, therefore, we examine data from Argo 2901469,
 368 which is located within AE2 during the period from 11 to 19 September. The temperature and salinity
 369 data from Station S5 is considered as the background, with S5 locates at a distance of 246 km from AE2's
 370 center on 15 September (Fig. 1). These profiles are categorized into three periods: pre-typhoon (11
 371 September), during-typhoon (15 September), and post-typhoon (19 September).

372 At depths above 40m, both inside and outside of AE2 experiences a decrease in temperature, with a
 373 cooling of less than -1.0°C . Four days after the typhoon passage (19 September), the cooling persists
 374 inside and outside the eddy, with the cooling being more pronounced outside AE2, showing a decrease
 375 of 1.2°C (Fig. 8c). The salinity within AE2 initially increases by 0.15 psu from the pre-typhoon stage to
 376 the during-typhoon stage and then decreases by 0.09 psu after the typhoon passage (Fig. 8d). While the
 377 salinity at Station 5 shows a similar pattern in pre-typhoon and during-typhoon stage, it increases by 0.05
 378 psu after the typhoon. Two possible processes can explain the difference in salinity trends inside and
 379 outside AE2. First, during the pre-typhoon to typhoon stage, the entrainment within AE2 may have
 380 brought the subsurface water, which is saltier, up to the surface, resulting in an increase in salinity. The

381 second process is related to the typhoon-induced precipitation after the typhoon passage, which lead to a
382 decrease in salinity. Strong stratification have contributed to the persistence of saltier subsurface water.
383 While at S5, the increase in salinity is relatively minor only increased slightly.

384 On 15 September, the subsurface layer at 45 m to 100 m is affected by the cold upwelling, which is
385 caused by the typhoon, resulting in a cooling and increased salinity within AE2. As the forcing of
386 Typhoon Kalmaegi diminishes, the upper layer of seawater begins to mix, and influences by the
387 downward flow of the eddy itself, warm surface water is transported to the subsurface layer. Four days
388 later, a warming phenomenon occurs, with the maximum warm anomaly of 1.2 °C observes at a depth of
389 75 m (Fig. 8a). The mixing effect outside the eddy is not significant, resulting in a slight subsurface
390 warming of approximately 0.2 °C, with no significant changes in salinity. However, on 19 September, a
391 maximum cold anomaly of -1.2°C is observed at a depth of 60 m, corresponding to the maximum salinity
392 anomaly of 0.13 psu (Fig. 8c-d). Below 100 m, AE2 experiences a temperature increase of 0.5 °C and a
393 slight decrease in salinity of 0.04 psu. On 19 September, the temperature and salinity within AE2 shows
394 little change. However, outside the eddy, a different response is observed. On 19 September, a cooling
395 trend is observed throughout the water column, within a range of 0.2 °C, accompanies by a noticeable
396 increase in salinity (Fig. 8c, d), within a range of 0.06 psu. This indicates that the typhoon causes a
397 significant upwelling outside the eddy region.



399 **Figure 8.** (a-b) the vertical profile of temperature and salt inside the eddy (Argo 2901469), (c-d) the vertical profiles
 400 of temperature and salt outside the eddy (S5). The red, black and blue lines represent pre-typhoon, during-typhoon
 401 and post-typhoon stages.

402 Based on Argo profiles and S5 data, the upper ocean above 200 m inside and outside AE2 responds
 403 differently to the forcing of the typhoon. In the upper layer (0-40 m), cooling is observed both inside and
 404 outside the eddy, and it lasts for a longer duration. In the subsurface layer (45-100m), after the passage
 405 of the typhoon (19 September), there is a strong cooling outside the eddy, while warming occurs within
 406 AE2. Zhang (2022) points out that the sea temperature anomalies mainly depend on the combined effects
 407 of mixing and vertical advection (cold suction). Mixing causes surface cooling and subsurface warming,
 408 while upwelling (downwelling) leads to cooling (warming) of the entire upper ocean. The temperature
 409 anomaly in the subsurface layer depends on the relative strength of mixing and vertical advection, with
 410 cold anomalies dominating when upwelling is strong, and downwelling amplifying the warming
 411 anomalies caused by mixing. Therefore, due to the strong influence of upwelling outside the eddy, the
 412 temperature profile of the entire water column shifts upwards, resulting in cooling of the entire upper
 413 ocean. On the other hand, influences by the downwelling associates with the warm eddy itself, a warming

414 anomaly of 1.2 °C is observed in the subsurface layer. Compares to region AE2, the cold suction effect
415 causes by the Typhoon Kalmaegi is still evident in the non-eddy area.

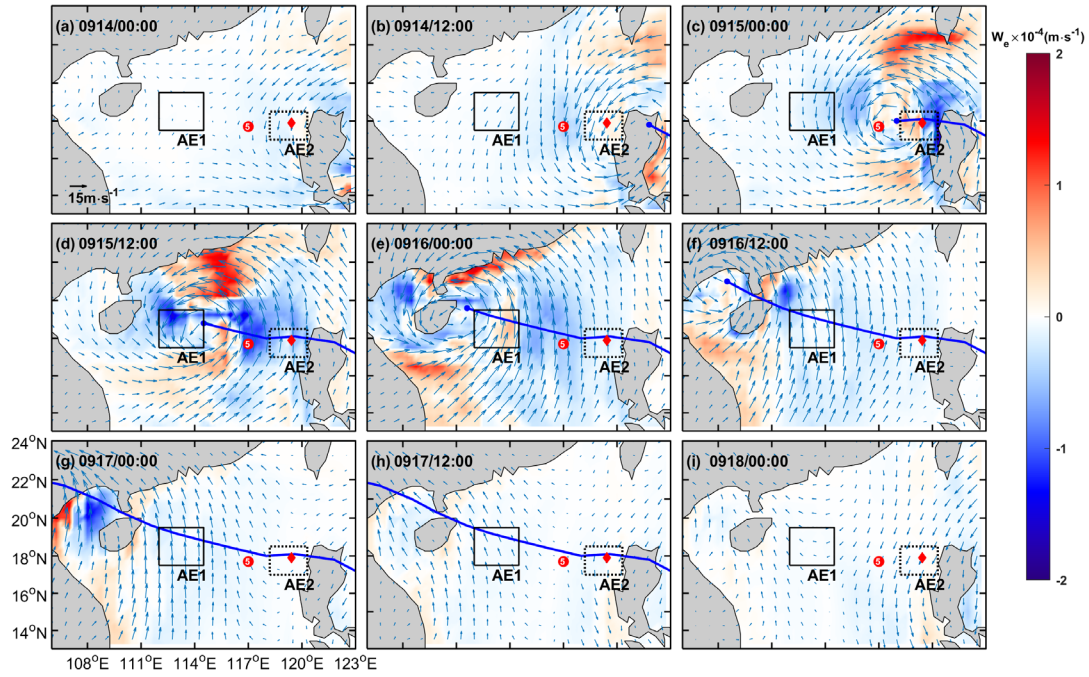
416 In the following sections, we delve into the underlying reasons behind these different responses of
417 AE1 and AE2 to Typhoon Kalmaegi.

418

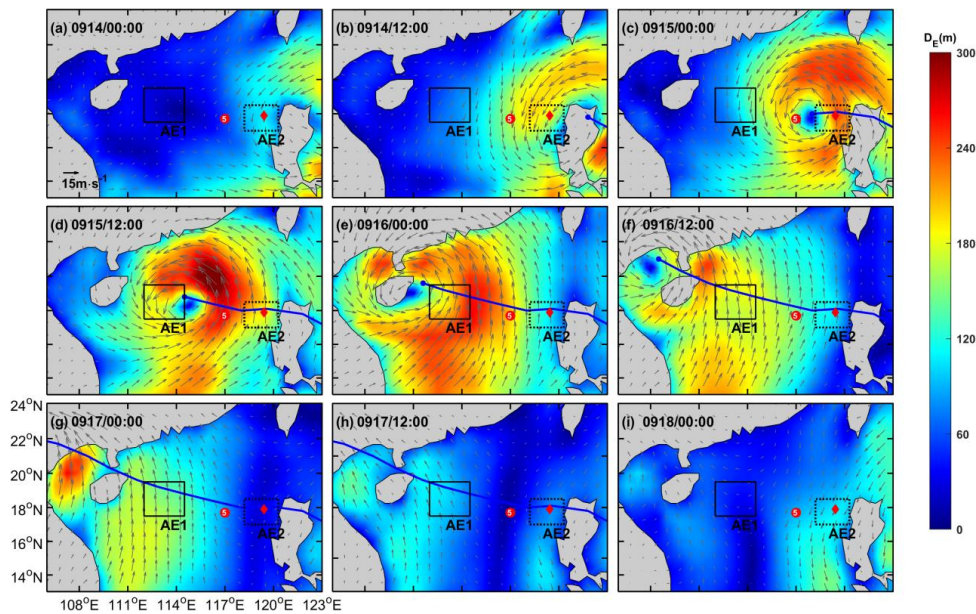
419 4. Discussion

420 The EPV is very small before the typhoon, measuring less than $0.5 \times 10^{-5} \text{ m.s}^{-1}$ in both AE1 and AE2.
421 However, during 15-16 September (Fig. 9c-f), when the typhoon crosses the NSCS, the EPV undergoes
422 significant changes. Its absolute value increases to over $1.5 \times 10^{-4} \text{ m.s}^{-1}$ within both AE1 and AE2. AE1
423 consistently exhibits a predominantly negative EPV during most of this period. Consequently, during
424 Typhoon Kalmaegi, the negative EPV facilitates downwelling and convergence (Jaimes and Shay, 2015),
425 leading to a warmer and fresher subsurface layer in AE1 (Fig. 6 a-b).

426 On the other hand, AE2 displays a more fluctuating pattern. It is positive on 14 September, shows
427 both positive and negative values at 0000 UTC on 15 September, and remains mainly negative from 15
428 to 16 September, and eventually returning to positive, reflecting a continuously fluctuating process. The
429 positive EPV in AE2 contributes to the influx of colder subsurface water into the upper layers, resulting
430 in surface and subsurface water cooling and an increase in salinity in the subsurface (Fig. 6c-d).
431 Correspondingly, the variations in Ekman layer depth (D_E) with the typhoon's passage are similar to EPV,
432 as shown in Fig. 10. When Kalmaegi approaches at 0000 UTC on 14 September, the mean D_E within
433 AE1 is only 21 m, while in AE2, it is 114 m. This indicates that AE2 has already been influenced by
434 Typhoon Kalmaegi. Subsequently, the depth of the DE within AE2 sharply deepens, reaching its
435 maximum depth of 241 m at 0000 UTC on 15 September, coinciding with the proximity of Typhoon
436 Kalmaegi's center to AE2. As Kalmaegi moves northwest, the D_E within AE1 achieves its maximum
437 depth of 262 m at 0000 UTC on 16 September. The trends of D_E within AE1 and AE2 are nearly
438 consistent, but AE1 lags behind AE2 by one day. Starting from 15 September, D_E within both AE1 and
439 AE2 gradually shallows, reaching a minimum D_E of 60 m. This value is 28 m higher than before the
440 typhoon, indicating the lingering effects of the typhoon through wind. For AE2, D_E reached its minimum
441 of 45 m at 0000 UTC on 18 September, later gradually increasing under the influence of tropical storm
442 Fung-wong.



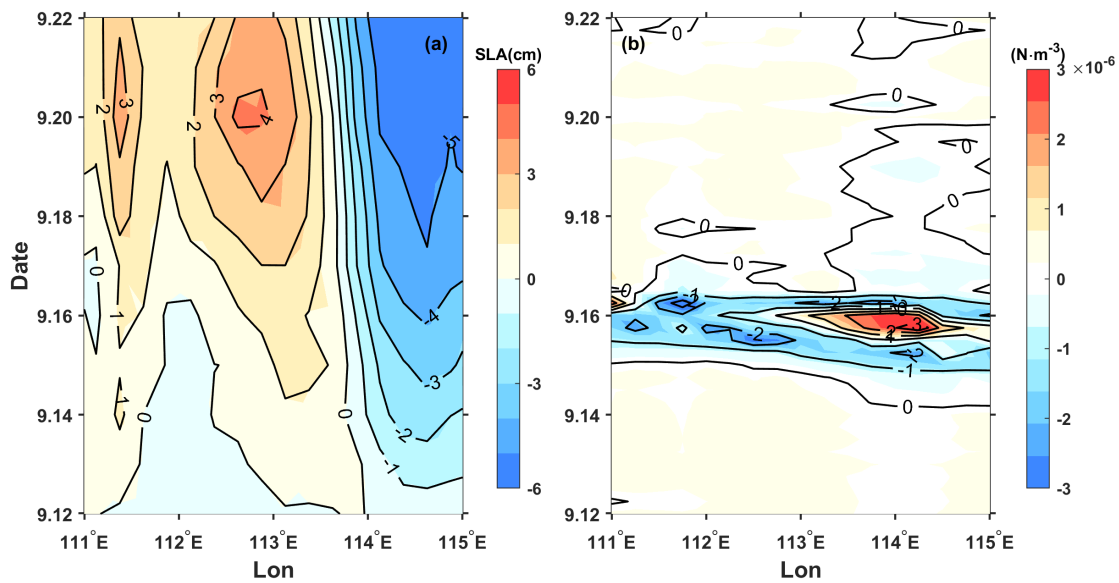
444 **Figure 9.** Ekman Pumping Velocity (EPV) from 14 September to 18 September (a-i). The color represents the EPV,
 445 the blue solid line is the path of Kalmaegi, the red dot and diamond are the positions of Station 5 and Argo 2901469
 446 on 15 September, respectively.



448 **Figure 10.** Ekman layer depth (D_E) from 14 September to 18 September (a-i). The color represents the D_E , the blue
 449 solid line is the path of Kalmaegi, the red dot and diamond are the positions of Station 5 and Argo 2901469 on 15
 450 September, respectively.

451 After traversing the warm ocean characteristics of AE2, Typhoon Kalmaegi strengthens, resulting in
 452 a reduction of the maximum wind radius. As it passed through AE1, the maximum wind radius is 35 km.
 453 Notably, the center of AE1 is located outside the typhoon's two-times maximum wind radius,
 454 approximately 104 km away from the typhoon center (Fig. 3). As mentioned earlier, strong upwelling
 455 occurs within two-times maximum wind radius, while weak subsidence exists in the vast area outside

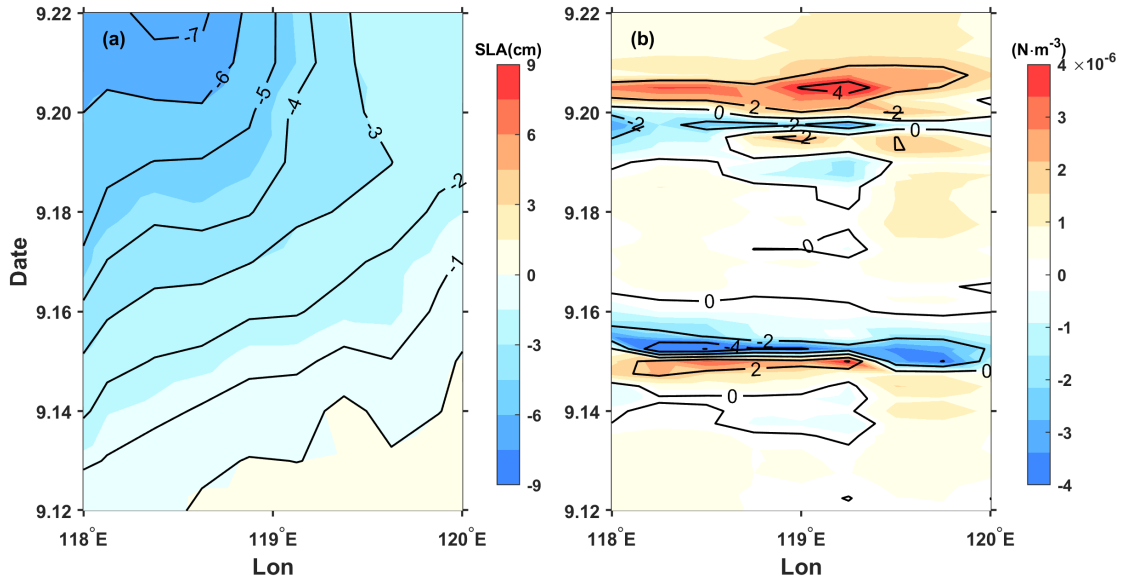
456 the upwelling region (Jaimes and Shay, 2015). Hence, the hypothesis presents here suggests that the
 457 observed intensification of AE1 on the left side of the typhoon track is more likely attributed to the
 458 negative wind stress generates outside the maximum wind radius, driving the enhancement of
 459 downwelling in the pre-existing anticyclonic feature in the ocean. Starting from 15 September, a
 460 significant positive sea level anomaly (SLA) to the west of 113.5°E becomes evident, intensifying and
 461 reaching its maximum on 20 September (Fig. 11a). This strengthening aligns with the increase in the
 462 amplitude of the warm core of the eddy AE1. A comparison with the wind stress curl anomaly (Fig. 11b)
 463 reveals that between 15 to 16 September, as the Typhoon Kalmaegi moves over the section at 18.2°N,
 464 specifically to the west of 113.5°E, it exhibits strong negative wind stress curl anomalies, with a
 465 maximum intensity of $-3 \times 10^{-6} \text{ N.m}^{-3}$. The negative wind stress curl induces by the typhoon results in
 466 favourable surface ocean currents that further enhances the clockwise rotation of the warm eddy. The
 467 negative wind stress curl anomaly results strong downwelling currents, inputting negative vorticity into
 468 AE1, leading to its intensification (Fig. 4b-c), as indicates by the enhanced positive SLA (Fig. 11a).
 469 Conversely, the region to the east of 113.5°E along the section exhibited negative SLA anomalies. This
 470 weakening is consistent with the previous observations of the intensified warm core and decreased eddy
 471 area.



473 **Figure 11.** The time/longitude plots of (a) SLA anomaly (cm) and (b) wind stress curl (N.m^{-3}) anomaly at the central
 474 section of AE1 (18.2°N). The anomalies were calculated relative to the average value of 10-13 September.

475 The response of AE2 differs from that of AE1 mainly because AE2 is quite near the Typhoon
 476 Kalmaegi's track. As the typhoon passes through AE2, the maximum wind radius is 48 km. AE2 is
 477 merely 26 km away from the typhoon center, essentially falling within two-times the maximum wind
 478 radius of the typhoon (Fig. 3). The significantly positive wind stress curl at the typhoon center induces
 479 upwelling and positive vorticity downward into the eddy (Huang and Wang, 2022), noticeably weakens
 480 the eddy, corresponding to the decrease in SLA (Fig. 12a). Furthermore, bases on the meridional isotherm
 481 profiles of the eddy center at three periods, it can be observed that during the passage of Typhoon
 482 Kalmaegi (15 September), the isotherms in the AE1 region exhibit significant subsidence (Fig. 13a),

483 while in the AE2 region, the isotherms show uplift (Fig. 13b). This result aligns with the earlier
 484 observation that the convergence and subsidence within the warm eddy AE1 are enhanced by the
 485 influence of the wind stress curl induced by the typhoon, while the intensity of AE2 is weakened.



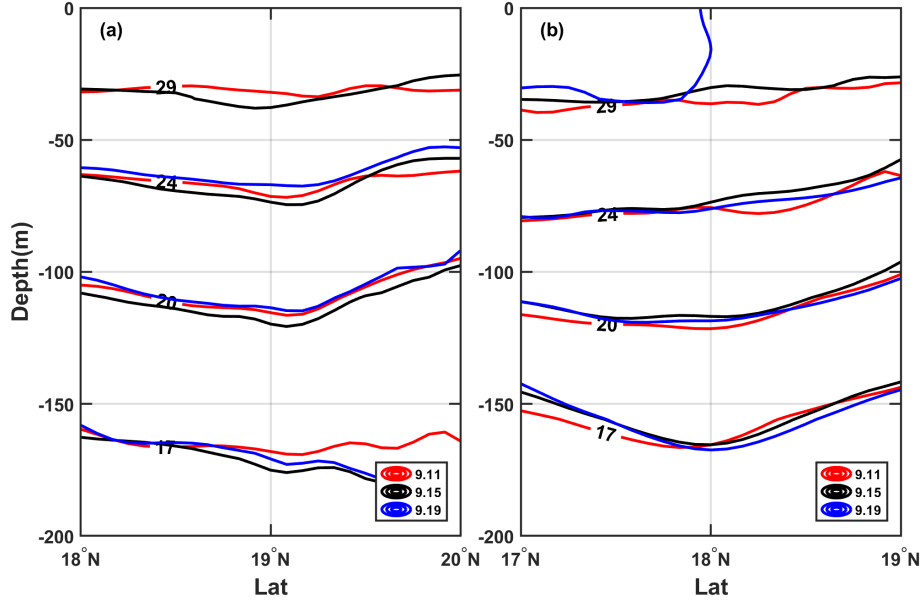
487 **Figure 12.** Same as Fig.10, but for AE2(17.9 °N).

488 From the above, the relative position of eddies and the typhoon can influence the response of the
 489 eddies (Lu et al., 2020). The warm eddy AE1, located on the left side of the typhoon track, is not
 490 weakened by the strong cold suction effect caused by the Typhoon Kalmaegi. Instead, it is strengthened
 491 due to the stronger negative wind stress curl generated by the typhoon.

492 To understand the work done by the Typhoon Kalmaegi on the eddies in the ocean, we estimate the
 493 total work inputted into the ocean current u_c using the previously calculated wind stress (Liu et al.,
 494 2017):

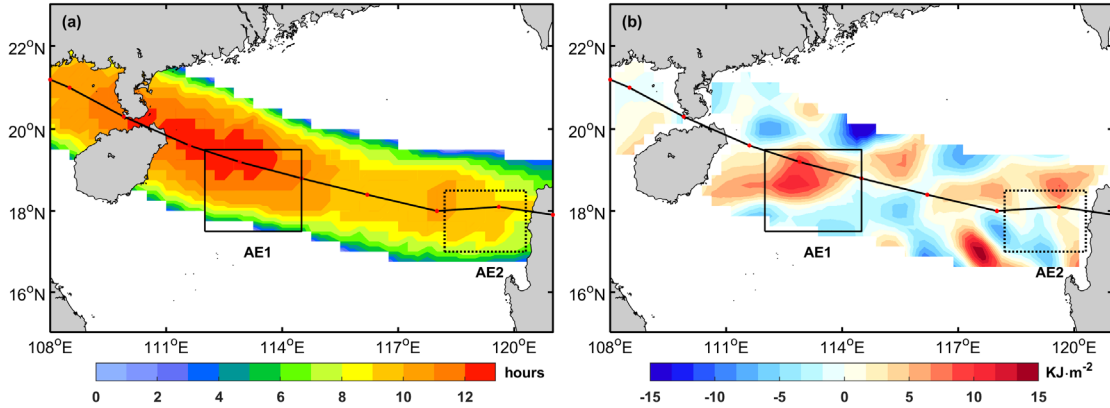
$$W = \int \vec{\tau} \cdot \vec{u}_c dt . \quad (10)$$

496 Here, we select the region near the typhoon track where the wind speed exceeds $17 \text{ m}\cdot\text{s}^{-1}$ as the typhoon
 497 forcing region to understand the energy input by the typhoon to the warm eddy (Sun et al., 2010). The
 498 forcing duration over the ocean in the typhoon-affected region and the work done by the typhoon on the
 499 surface current are shown in Fig. 13. When the angle between the wind and the ocean current is acute,
 500 the typhoon does positive work on the ocean current. Conversely, when the angle is obtuse, the typhoon
 501 does negative work on the ocean current. It is evident that the region with the maximum forcing duration
 502 by the typhoon on AE1 corresponds to the area where the typhoon clearly does positive work on the
 503 ocean current, accumulating a work done exceeding 8 KJ m^{-2} . This acceleration of the flow velocity in
 504 the eddy results in convergence within the eddy and an increase in SLA, leading to the strengthening of
 505 AE1. On the other hand, the forcing duration by the typhoon on AE2 is smaller, and the typhoon does
 506 negative work on the ocean current in most areas, with a cumulative work done within -5 KJ m^{-2} , causing
 507 the flow velocity within the AE2 to decelerate.



509 **Figure 13.** The meridional isotherm profiles of AE1 (a) and AE2 (b) before (11 September), during (15 September)
 510 and after (19 September) Typhoon Kalmaegi.

511



513 **Figure 14.** (a): the forcing time (unit: hours) of the typhoon; (b): the input work (unit: $\text{KJ} \cdot \text{m}^{-2}$) of the typhoon to
 514 the current.

515 **5. Summary**

516 Based on multi-satellite observations, on-site measurements, and numerical model data, we have
 517 gained valuable insights into the response of warm eddies AE1 and AE2 in the northern South China Sea
 518 to Typhoon Kalmaegi. Both horizontally and vertically, these eddies display distinct differences.
 519 Horizontally, we observe a reduction of areas by approximately 31% (AE1) and 36% (AE2). AE1,
 520 positions on the left side of the typhoon's track, strengthens with amplitude, R_o and EKE increasing by
 521 1.3 cm, 1.4×10^{-2} and $107.2 \text{ cm}^2 \cdot \text{s}^{-2}$ after the typhoon passed. In contrast, AE2, which intersects with the
 522 typhoon's track, weakens with amplitude, R_o and EKE decreasing by 3.1 cm, 1.6×10^{-2} and $38.5 \text{ cm}^2 \cdot \text{s}^{-2}$,
 523 respectively. Vertically, during the typhoon's passage, AE1 experiences intensified converging
 524 subsidence flow at its center, leading to an increase in temperature and a decrease in salinity above 150
 525 m. This response is more pronounced below the MLD (1.3°C) and persists for about a week after the

526 typhoon. On the other hand, AE2 exhibits cooling above the MLD, accompanied by a decrease in salinity,
527 as well as a subsurface temperature drop and salinity increase due to the upwelling of cold water caused
528 by the typhoon's suction effect. The subsurface cooling and salinity increase in AE2 are further
529 influenced by Typhoon Fung-wong. Additionally, from the temperature vertical profile of Argo and in-
530 situ arrays, on 19 September, it can be seen that the non-eddy region also experiences significant cooling,
531 with a prominent cooling center observed at a depth of 60 m ($-1.2\text{ }^{\circ}\text{C}$). The warm eddy AE2, influenced
532 by its own downwelling, exhibits enhanced mixing effects, resulting in a subsurface warm anomaly of
533 $1.2\text{ }^{\circ}\text{C}$.

534 Further analysis reveals that the different responses of the warm eddies can be attributed to factors
535 such as wind stress curl distribution, which are influenced by the relative position of the warm eddies
536 and the typhoon track. The wind stress curl induced by the typhoon plays a crucial role in shaping the
537 response of the warm eddies. AE1, located on the left side of the typhoon's path, experiences prolonged
538 forcing from the typhoon, resulting in positive work on the ocean current. This inputs a strong negative
539 wind stress curl into the eddy, enhancing negative EPV and deepening D_E , so the downwelling within
540 the AE1 is obvious and contributing to its increased strength. In contrast, AE2, positioned directly below
541 the typhoon's track, experiences shorter forcing duration and weakens due to the strong positive wind
542 stress curl at the typhoon's center and shallower D_E . Furthermore, the absolute value of EPV increases in
543 both warm eddies during the typhoon's passage, but with differing impacts. The positive EPV contributes
544 to surface water cooling and the influx of cooler subsurface water, while the negative EPV facilitates
545 downwelling and intensifies the influence of the warm eddies.

546 While numerous prior studies exploring the interaction between TCs and eddies have predominantly
547 drawn generalized conclusions, such as the weakening (strengthening) effect of cold (warm) eddies.
548 Conversely, TCs are recognized for strengthening cold eddies and weakening warm eddies. However,
549 our study takes a different approach. We aim to illustrate that even when TCs encounter eddies of the
550 same polarity, the response of these eddies to TCs exhibits variations. This nuanced response is intricately
551 linked to factors including the relative position of the eddies and the TCs, the eddies' intensity, and the
552 background current. It is discussed for the first time in the South China Sea. By analyzing wind stress curl
553 distribution, EPV, buoyancy frequency and the relative position between the eddies and the typhoon's
554 track, this case study provides a more nuanced understanding of the mechanisms driving these different
555 eddy-typhoon interactions in the Northern South China Sea. Moreover, it will further improve the
556 accuracy of TC forecasts and enhance the simulation capabilities of air-sea coupled models.

557

558 *Data availability.* The six-hourly best-track typhoon datasets were accessed on 3 February 2021 by JTWC,
559 <http://www.usno.navy.mil/JTWC>, JMA, <https://www.jma.go.jp/jma/jma-eng/jma-center/rsmc-hp-pub-eg/besttrack.html> and CMA, <http://tcdata.typhoon.gov.cn>. The AVISO product was accessed on 14 February
560 2021 by <https://marine.copernicus.eu/>. The AVHRR SST data was accessed on 16 March, 2022 by
561 ftp://podaac.jpl.nasa.gov/documents/dataset_docs/avhrr_pathfinder_sst.html. The Argo data was accessed
562 on 4 April, 2022 by <https://dataselection.euro-argo.eu/>. The wind data was accessed on 5 January, 2023 by

564 <https://apps.ecmwf.int/datasets/data/interim-full-daily/levtype=sfc/>. The GLORYS12V1 was accessed on
565 23 March, 2022 by <https://marine.copernicus.eu/>.

566 *Author contributions.* XYL and HZ contributed to the study conception and design. Material preparation, data
567 collection and analysis were performed by YHH and XYL. GQH and YL contributed to the methodology. The
568 original manuscript was prepared by XYL and YHH. All the authors contributed to the review and editing of
569 the manuscript.

570 *Competing interests.* The contact author has declared that none of the authors has any competing interests.

571 *Disclaimer.* Publisher's note: Copernicus Publications remains neutral with regard to jurisdictional claims in
572 published maps and institutional affiliations.

573 *Acknowledgements.* These data were collected and made freely available by JTCW, JMA, CMA, AVISO, AVHRR,
574 Argo, ECMWF, COPERNICUS. All figures were created using MATLAB, in particular using the M_Map toolbox
575 (Pawlowicz, 2020). The authors thank the anonymous reviewers, whose feedback led to substantial im-
576 provement of the resulting analyses, figures and manuscript

577 *Financial support.* This research has been supported by the National Natural Science Foundation of China
578 (42227901), Southern Marine Science and Engineering Guangdong Laboratory (Zhuhai), grant number
579 SML2020SP007 and SML2021SP207; the Innovation Group Project of Southern Marine Science and
580 Engineering Guangdong Laboratory (Zhuhai), grant number 311020004 and 311022001; the National
581 Natural Science Foundation of China, grant number 42206005; the open fund of State Key Laboratory of
582 Satellite Ocean Environment Dynamics, Second Institute of Oceanography, MNR, grant number QNHX2309;
583 General scientific research project of Zhejiang Provincial Department of Education, grant number
584 Y202250609; the Open Foundation from Marine Sciences in the First-Class Subjects of Zhejiang, grant number
585 OFMS006; State Key Laboratory of Tropical Oceanography (South China Sea Institute of Oceanology Chinese
586 Academy of Sciences), grant number LTO2220.

587

588

589

590 **References**

591 Cabanes, C., Grouazel, A., von Schuckmann, K., Hamon, M., Turpin, V., Coatanoan, C., Guinehut, S.,
592 Boone, C., Ferry, N., and Reverdin, G.: The CORA dataset: validation and diagnostics of ocean
593 temperature and salinity in situ measurements, *Ocean Sci. Discuss.*, 9, 1273-1312, 2012.
594 Chen, G., Hou, Y., and Chu, X.: Mesoscale eddies in the South China Sea: Mean properties,
595 spatiotemporal variability, and impact on thermohaline structure, *J. Geophys. Res.: Oceans*,
596 116, <https://doi.org/10.1029/2010jc006716>, 2011.

597 Chen Z, Yu F, Chen Z, et al. Downward Propagation and Trapping of Near-Inertial Waves by a
598 Westward-moving Anticyclonic Eddy in the Subtropical Northwestern Pacific Ocean[J]. *Journal of*
599 *Physical Oceanography*, 2023.

600 de Boyer Montégut, C.: Mixed layer depth over the global ocean: An examination of profile data and a
601 profile-based climatology, *J. Geophys. Res.: Oceans*, 109,<https://doi.org/10.1029/2004jc002378>, 2004.

602 Ezraty, R., Girard-Ardhuin, F., Piollé, J.-F., Kaleschke, L., and Heygster, G.: Arctic and Antarctic sea
603 ice concentration and Arctic sea ice drift estimated from Special Sensor Microwave data, Département
604 d’Océanographie Physique et Spatiale, IFREMER, Brest, France and University of Bremen Germany, 2,
605 2007.

606 Huang, L., Cao, R., and Zhang, S.: Distribution and Oceanic Dynamic Mechism of Precipitation Induced
607 by Typhoon Lekima, *American Journal of Climate Change*, 11, 133-
608 154,<https://doi.org/10.4236/ajcc.2022.112007>, 2022.

609 Huang, X. and Wang, G.: Response of a Mesoscale Dipole Eddy to the Passage of a Tropical Cyclone:
610 A Case Study Using Satellite Observations and Numerical Modeling, *Remote Sens.*,
611 14,<https://doi.org/10.3390/rs14122865>, 2022.

612 Jaimes, B. and Shay, L. K.: Enhanced Wind-Driven Downwelling Flow in Warm Oceanic Eddy Features
613 during the Intensification of Tropical Cyclone Isaac (2012): Observations and Theory, *J. Phys. Oceanogr.*,
614 45, 1667-1689,<https://doi.org/10.1175/jpo-d-14-0176.1>, 2015.

615 Jullien, S., Menkès, C. E., Marchesiello, P., Jourdain, N. C., Lengaigne, M., Koch-Larrouy, A., Lefèvre,
616 J., Vincent, E. M., and Faure, V.: Impact of tropical cyclones on the heat budget of the South Pacific
617 Ocean, *J. Phys. Oceanogr.*, 42, 1882-1906,<https://doi.org/10.1175/JPO-D-11-0133.1>, 2012.

618 Kessler, W. S.: The circulation of the eastern tropical Pacific: A review, *Prog. Oceanogr.*, 69, 181-
619 217,<https://doi.org/10.1016/j.pocean.2006.03.009>, 2006.

620 Li, Q., Sun, L., Liu, S., Xian, T., and Yan, Y.: A new mononuclear eddy identification method with
621 simple splitting strategies, *Remote Sens. Lett.*, 5, 65 - 72,<https://doi.org/10.1080/2150704x.2013.872814>,
622 2014.

623 Li, X., Zhang, X., Fu, D., and Liao, S.: Strengthening effect of super typhoon Rammasun (2014) on
624 upwelling and cold eddies in the South China Sea, *J. Oceanol. Limnol.*, 39, 403-
625 419,<https://doi.org/10.1007/s00343-020-9239-x>, 2021.

626 Lin, I. I., Chou, M.-D., and Wu, C.-C.: The Impact of a Warm Ocean Eddy on Typhoon Morakot (2009):
627 A Preliminary Study from Satellite Observations and Numerical Modelling, *TAO: Terrestrial,*
628 *Atmospheric and Oceanic Sciences*, 22,[https://doi.org/10.3319/tao.2011.08.19.01\(tm\)](https://doi.org/10.3319/tao.2011.08.19.01(tm)), 2011.

629 Lin, I. I., Wu, C.-C., Emanuel, K. A., Lee, I. H., Wu, C.-R., and Pun, I.-F.: The Interaction of
630 Supertyphoon Maemi (2003) with a Warm Ocean Eddy, *Mon. Weather Rev.*, 133, 2635-
631 2649,<https://doi.org/10.1175/MWR3005.1>, 2005.

632 Liu, F. and Tang, S.: Influence of the Interaction Between Typhoons and Oceanic Mesoscale Eddies on
633 Phytoplankton Blooms, *J. Geophys. Res.: Oceans*, 123, 2785-
634 2794,<https://doi.org/10.1029/2017jc013225>, 2018.

635 Liu, S.-S., Sun, L., Wu, Q., and Yang, Y.-J.: The responses of cyclonic and anticyclonic eddies to
636 typhoon forcing: The vertical temperature-salinity structure changes associated with the horizontal
637 convergence/divergence, *J. Geophys. Res.: Oceans*, 122, 4974-
638 4989,<https://doi.org/10.1002/2017JC012814>, 2017.

639 Lu, Z., Wang, G., and Shang, X.: Response of a Preexisting Cyclonic Ocean Eddy to a Typhoon, *J. Phys.*
640 *Oceanogr.*, 46, 2403-2410,<https://doi.org/10.1175/jpo-d-16-0040.1>, 2016.

641 Lu, Z., Wang, G., and Shang, X.: Strength and Spatial Structure of the Perturbation Induced by a Tropical
642 Cyclone to the Underlying Eddies, *J. Geophys. Res.: Oceans*, 125,<https://doi.org/10.1029/2020jc016097>,
643 2020.

644 Lu, Z., Wang, G., and Shang, X.: Observable large-scale impacts of tropical cyclones on subtropical gyre,
645 *J. Phys. Oceanogr.*,<https://doi.org/10.1175/JPO-D-22-0230.1>, 2023.

646 Ma, Z., Zhang, Z., Fei, J., and Wang, H.: Imprints of Tropical Cyclones on Structural Characteristics of
647 Mesoscale Oceanic Eddies Over the Western North Pacific, *Geophys. Res. Lett.*,
648 48,<https://doi.org/10.1029/2021gl092601>, 2021.

649 Ma, Z., Fei, J., Liu, L., Huang, X., and Li, Y.: An Investigation of the Influences of Mesoscale Ocean
650 Eddies on Tropical Cyclone Intensities, *Mon. Weather Rev.*, 145, 1181-
651 1201,<https://doi.org/10.1175/mwr-d-16-0253.1>, 2017.

652 Ning, J., Xu, Q., Zhang, H., Wang, T., and Fan, K.: Impact of Cyclonic Ocean Eddies on Upper Ocean
653 Thermodynamic Response to Typhoon Soudelor, *Remote Sens.*, 11,<https://doi.org/10.3390/rs11080938>,
654 2019.

655 Oey, L. Y., Ezer, T., Wang, D. P., Fan, S. J., and Yin, X. Q.: Loop Current warming by Hurricane Wilma,
656 *Geophys. Res. Lett.*, 33,<https://doi.org/10.1029/2006gl025873>, 2006.

657 Price, J. F.: Upper Ocean Response to a Hurricane, *J. Phys. Oceanogr.*,[https://doi.org/10.1175/1520-0485\(1981\)011%3C0153:UORTAH%3E2.0.CO;2](https://doi.org/10.1175/1520-0485(1981)011%3C0153:UORTAH%3E2.0.CO;2), 1981.

659 Pujol, M.-I., Faugère, Y., Taburet, G., Dupuy, S., Pelloquin, C., Ablain, M., and Picot, N.: DUACS
660 DT2014: the new multi-mission altimeter data set reprocessed over 20 years, *Ocean Sci.*, 12, 1067-
661 1090,<https://doi.org/10.5194/os-12-1067-2016>, 2016.

662 Rudzin, J. E. and Chen, S.: On the dynamics of the eradication of a warm core mesoscale eddy after the
663 passage of Hurricane Irma (2017), *Dyn. Atmos. Oceans*,
664 100,<https://doi.org/10.1016/j.dynatmoce.2022.101334>, 2022.

665 Shang, X.-d., Zhu, H.-b., Chen, G.-y., Xu, C., and Yang, Q.: Research on Cold Core Eddy Change and
666 Phytoplankton Bloom Induced by Typhoons: Case Studies in the South China Sea, *Adv. Meteorol.*, 2015,
667 1-19,<https://doi.org/10.1155/2015/340432>, 2015.

668 Shay, L. K. and Jaimes, B.: Mixed Layer Cooling in Mesoscale Oceanic Eddies during Hurricanes
669 Katrina and Rita, *Mon. Weather Rev.*, 137, 4188-4207,<https://doi.org/10.1175/2009mwr2849.1>, 2009.

670 Shay, L. K. and Jaimes, B.: Near-Inertial Wave Wake of Hurricanes Katrina and Rita over Mesoscale
671 Oceanic Eddies, *J. Phys. Oceanogr.*, 40, 1320-1337,<https://doi.org/10.1175/2010jpo4309.1>, 2010.

672 Shay, L. K., Goni, G. J., and Black, P. G.: Effects of a Warm Oceanic Feature on Hurricane Opal, *Mon.*
673 *Weather Rev.*, 128, 1366-1383,[https://doi.org/10.1175/1520-0493\(2000\)128<1366:EOAWOF>2.0.CO;2](https://doi.org/10.1175/1520-0493(2000)128<1366:EOAWOF>2.0.CO;2), 2000.

675 Song, D., Guo, L., Duan, Z., and Xiang, L.: Impact of Major Typhoons in 2016 on Sea Surface Features
676 in the Northwestern Pacific, *Water*, 10,<https://doi.org/10.3390/w10101326>, 2018.

677 Sun, J., Ju, X., Zheng, Q., Wang, G., Li, L., and Xiong, X.: Numerical Study of the Response of Typhoon
678 Hato (2017) to Grouped Mesoscale Eddies in the Northern South China Sea, *J. Geophys. Res.: Atmos.*,
679 128,<https://doi.org/10.1029/2022jd037266>, 2023.

680 Sun, L., Yang, Y., Xian, T., Lu, Z., and Fu, Y.: Strong enhancement of chlorophyll a concentration by a
681 weak typhoon, *Mar. Ecol. Prog. Ser.*, 404, 39-50,<https://doi.org/10.3354/meps08477>, 2010.

682 Sun, L., Li, Y.-X., Yang, Y.-J., Wu, Q., Chen, X.-T., Li, Q.-Y., Li, Y.-B., and Xian, T.: Effects of super
683 typhoons on cyclonic ocean eddies in the western North Pacific: A satellite data-based evaluation

684 between 2000 and 2008, *J. Geophys. Res.: Oceans*, 119, 5585-
685 5598,<https://doi.org/10.1002/2013jc009575>, 2014.

686 Thompson, B. and Tkalich, P.: Mixed layer thermodynamics of the Southern South China Sea, *Clim.*
687 *Dyn.*, 43, 2061-2075,<https://doi.org/10.1007/s00382-013-2030-3>, 2014.

688 Wada, A. and Usui, N.: Impacts of Oceanic Preexisting Conditions on Predictions of Typhoon Hai-Tang
689 in 2005, *Adv. Meteorol.*, 2010, 756071,<https://doi.org/10.1155/2010/756071>, 2010.

690 Walker, N. D., Leben, R. R., and Balasubramanian, S.: Hurricane-forced upwelling and
691 chlorophyllaenhancement within cold-core cyclones in the Gulf of Mexico, *Geophys. Res. Lett.*, 32, n/a-
692 n/a,<https://doi.org/10.1029/2005gl023716>, 2005.

693 Wang, G., Su, J., Ding, Y., and Chen, D.: Tropical cyclone genesis over the south China sea, *J. Mar.*
694 *Syst.*, 68, 318-326,<https://doi.org/10.1016/j.jmarsys.2006.12.002>, 2007.

695 Wang, G., Zhao, B., Qiao, F., and Zhao, C.: Rapid intensification of Super Typhoon Haiyan: the
696 important role of a warm-core ocean eddy, *Ocean Dyn.*, 68, 1649-1661,<https://doi.org/10.1007/s10236-018-1217-x>, 2018.

698 Xiu, P., Chai, F., Shi, L., Xue, H., and Chao, Y.: A census of eddy activities in the South China Sea
699 during 1993–2007, *J. Geophys. Res.: Oceans*, 115,<https://doi.org/10.1029/2009jc005657>, 2010.

700 Yan, Y., Li, L., and Wang, C.: The effects of oceanic barrier layer on the upper ocean response to tropical
701 cyclones, *J. Geophys. Res.: Oceans*, 122, 4829-4844,<https://doi.org/10.1002/2017jc012694>, 2017.

702 Yu, F., Yang, Q., Chen, G., and Li, Q.: The response of cyclonic eddies to typhoons based on satellite
703 remote sensing data for 2001–2014 from the South China Sea, *Oceanologia*, 61, 265-
704 275,<https://doi.org/10.1016/j.oceano.2018.11.005>, 2019.

705 Yu, J., Lin, S., Jiang, Y., and Wang, Y.: Modulation of Typhoon-Induced Sea Surface Cooling by
706 Preexisting Eddies in the South China Sea, *Water*, 13,<https://doi.org/10.3390/w13050653>, 2021.

707 Zhang, H.: Modulation of Upper Ocean Vertical Temperature Structure and Heat Content by a Fast-
708 Moving Tropical Cyclone, *J. Phys. Oceanogr.*, 53, 493-508,<https://doi.org/10.1175/jpo-d-22-0132.1>,
709 2022.

710 Zhang, H., Chen, D., Zhou, L., Liu, X., Ding, T., and Zhou, B.: Upper ocean response to typhoon
711 Kalmaegi (2014), *J. Geophys. Res.: Oceans*, 121, 6520-6535,<https://doi.org/10.1002/2016jc012064>,
712 2016.

713 Zhang, Y., Zhang, Z., Chen, D., Qiu, B., and Wang, W.: Strengthening of the Kuroshio current by
714 intensifying tropical cyclones, *Science*, 368, 988-993,<https://doi.org/10.1126/science.aax5758>, 2020.

715